




High-frequency diode effect in superconducting Nb₃Sn microbridges

Sara Chahid , Serafim Teknowijoyo, Iris Mowgood , and Armen Gulian ^{*}

Advanced Physics Laboratory, Institute for Quantum Studies, Chapman University, Burtonsville, Maryland 20866, USA



(Received 6 January 2023; revised 3 February 2023; accepted 6 February 2023; published 22 February 2023)

The superconducting diode effect has recently been reported in a variety of systems and different symmetry-breaking mechanisms have been examined. However, the frequency range of these potentially important devices still remains obscure. We investigated superconducting microbridges of Nb₃Sn in out-of-plane magnetic fields; optimum magnetic fields of ~ 10 mT generate $\sim 10\%$ diode efficiency, while higher fields of ~ 15 – 20 mT quench the effect. The diode changes its polarity with magnetic field reversal. We documented superconductive diode rectification at frequencies up to 100 kHz, the highest reported as of today. Interestingly, the bridge resistance during diode operation reaches a value that is a factor of two smaller than in its normal state, which is compatible with the vortex-caused mechanism of resistivity. This is confirmed by finite-element modeling based on time-dependent Ginzburg-Landau equations. To explain experimental findings, no assumption of lattice thermal inequilibrium has been required. Dissimilar edges of the superconductor strip can be responsible for the inversion symmetry breaking by the vortex penetration barrier; visual evidence of this opportunity was revealed by scanning electron microscopy. Estimates are in favor of a much higher (GHz) range of frequencies for this type of diode.

DOI: [10.1103/PhysRevB.107.054506](https://doi.org/10.1103/PhysRevB.107.054506)

I. INTRODUCTION

For certain important problems of fundamental physics, such as the exploration of possible quasilocal action of curl-less vector potential [1], it is necessary to explore superconducting microbridges for assurance that the magnitudes of the critical currents of the bridge are equal for both current polarities. In particular, accidental breaking of time-reversal symmetry (TRS) by remanent or spurious magnetic fields in the cryostat, together with simultaneous inversion symmetry (IS) breaking by, e.g., physical asymmetry of the bridge edges, can cause the superconducting diode effect (SDE), which violates this equality [2–9]. Actually, in certain cases (see, e.g., [8,10–12]), nonreciprocal transport has been predicted and claimed experimentally even in the absence of TRS [13]. While this equality violation should be avoided for the above-mentioned task [1], it is underlying for the SDE.

Recently, the SDE attracted noticeable attention within the research community [2–9,14–26], and the related activity generated multiple mechanisms applicable to understanding the SDE. In theoretical models, the TRS is broken by an externally applied magnetic field or internal inclusions of magnetic microclusters, while the IS is broken by the out-of-plane Rashba spin-orbit coupling [18,19,21–23], valley-Zeeman interaction [17], etc., which results in the emergence of a helical superconductivity [18,19,21,23]. Experimentally, systems based on van der Waals material MoS₂ with noncentrosymmetric crystal potential [14], synthetic superlattice of Nb/V/Ta [5], and intrinsically IS broken NbSe₂ [15] have been reported, as well as planar Josephson junction arrays

of Al on InAs [7,16]. Yet other systems reveal nonreciprocal behavior in field-free environments, such as NbSe₂-based Josephson junction [8], trilayer graphene [20], and Josephson junction based on chiral superconductor Sr₂RuO₄ with the internally broken TRS [24]. In view of a variety of experimental observations and theories on the SDE in systems of different configurations, it is quite reasonable to assume that more than one mechanism can be responsible for the ubiquity of nonreciprocity observations in superconductor thin films [27]. In a recent article [28], the SDE was found in NbN microbridges in an out-of-plane magnetic field. This observation was attributed to the critical current being determined by the vortex flow, confirming that the SDE is caused by unequal vortex barriers on the two edges of the bridge [29,30].

To understand this mechanism, consider a type-II superconductor film strip. A magnetic field above a certain critical value creates vortices; initially, they nucleate at the strip edges [31,32]. The morphology of these edges affects the surface barrier, which prevents the vortices from entering into the strip [33,34]. However, if the current through the strip is strong enough, the Lorentz force which it exerts onto the vortices overcomes the surface barrier; vortices start moving across the strip, thus dissipating energy and creating a resistive state. In practice, vortex barriers are unequal because of the nonidentical structure of the strip edges. This circumstance was used by Vodolazov and Peeters [30] when predicting the SDE in 2005. It was experimentally observed recently [28], though the closely related ratcheting effect was reported as early as 2003 [35] (see, also, [36–39]).

The spike of activities in the area of superconducting diodes paves the way towards future practical application of these novel devices in superconducting electronics. However, a very important topic is still open and remains mainly unad-

^{*}Corresponding author: gulian@chapman.edu

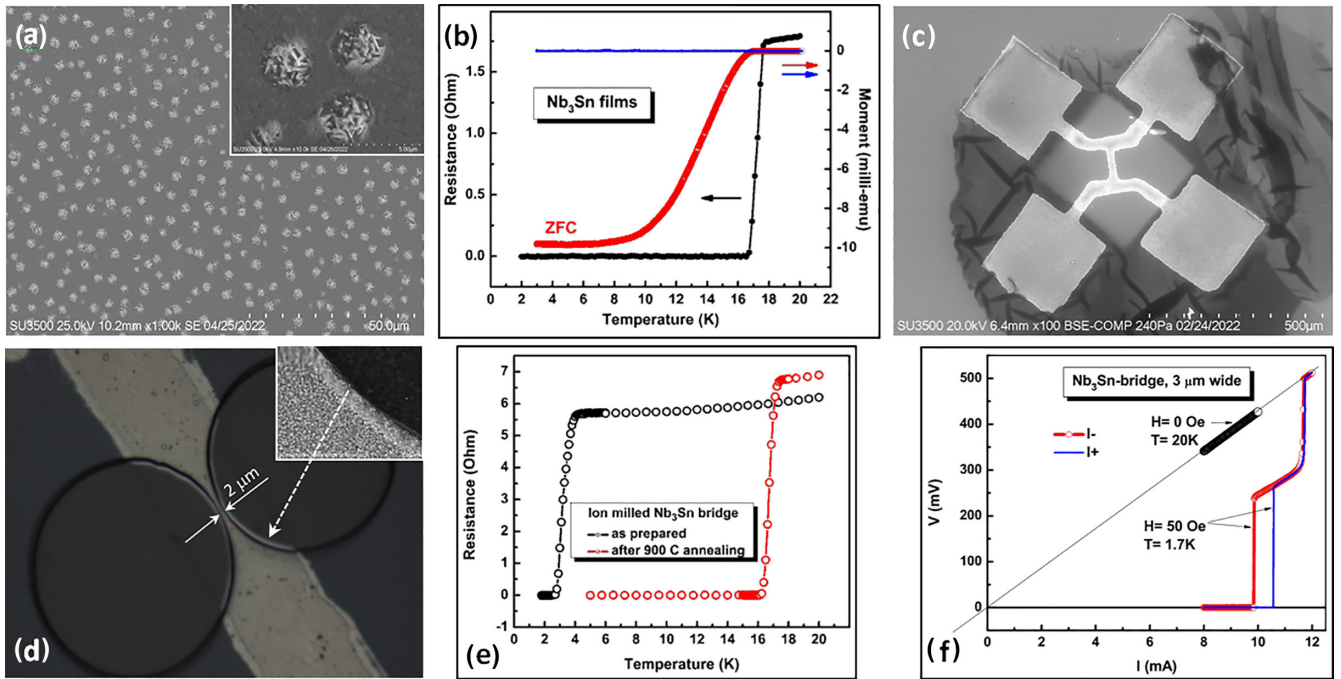


FIG. 1. (a) Surface morphology of the films with inclusion of small areas (nanomountains) with higher concentration of Sn (zoomed 10-fold in the inset). (b) Resistive and magnetic transitions into superconducting state. (c) A bridge after ion milling of three-dimensional (3D)-printed pattern (initial stage of preparation). (d) Last stage of bridge preparation: the structure in panel (c) was covered by positive photoresist, and two circles were projected via an epifluorescent microscope and ion milled to reduce the active part of the bridges to a micronscale (the smallest, 2 μm , result is shown). Inset illustrates the microroughness of the edge line. (e) Effects of ion milling and postannealing on the transition temperature of bridges. (f) Typical voltage-current dependence of bridges above ($T = 20\text{ K}$) and well below ($T = 1.7\text{ K}$) the superconducting transition.

dressed: the frequency range of the SDE. In the report by Lyu *et al.* [40], experiments have been performed at 30 kHz; however, the diode outputs were acquired by a DC nanovoltmeter, which leaves the dynamics of the device obscure. Here, we directly detect the voltage response in the time domain at frequencies up to 100 kHz. Experimental findings and modeling results provide us with the grounds to conclude that the SDE can perform at much higher frequencies.

II. EXPERIMENTAL DETAILS

Our study used conventional Nb_3Sn superconducting thin-film bridges. The Nb_3Sn films were prepared in a DC/RF magnetron sputtering system (manufactured by AJA International, Inc.) with a base pressure of 1×10^{-8} Torr. The Nb target (Kurt Lesker, 99.95%) was placed inside a DC gun, while the Sn target (Kurt Lesker, 99.999%) was sputtered using an RF source to avoid melting. The sapphire substrate (AdValue Technology, thickness 650 μm , C cut) was cleaned thoroughly with isopropyl alcohol before it was mounted on the holder. In our chamber's configuration, the substrate holder is at the center of the chamber facing upwards, while the (five) sputtering guns are located at the top. The substrate is rotated in plane throughout the whole deposition process to ensure a homogeneous deposition layer over the whole surface. Our predeposition *in situ* cleaning of the substrate involves heating it up to 900 $^\circ\text{C}$ for 10 min followed by a gentle bombardment of Ar^+ ions at 400 $^\circ\text{C}$ for 5 min. The

substrate was oriented to face the ion gun squarely. For the Nb_3Sn film deposition, we used a “stack+anneal” process similar to the one in [41]. Taking advantage of the Nb-Sn phase diagram [42], an alternating Nb and Sn stacks with an excess Sn content (Nb:Sn ratio ~ 2) “phase locks” into the Nb_3Sn composition when the excess Sn evaporates during postdeposition annealing. For the first/base layer, Nb was sputtered in DC mode with 500 W power and 3 mTorr pressure at 600 $^\circ\text{C}$ for 20 min. Then, the Sn layer was deposited on top of Nb in RF mode with 250 W power and 30 mTorr pressure at 100 $^\circ\text{C}$ for 15 min. Nb was deposited one more time as the capping (third) layer using the same parameters as the base layer for 3 min. Finally, the substrate was heated *in situ* to 950 $^\circ\text{C}$ for 30 min to let the excess Sn evaporate before cooling down to room temperature. All the heating/cooling protocols consistently used a 30 $^\circ\text{C}/\text{min}$ ramp rate. Our films are $\sim 100\text{ nm}$ thick and resistivity measurements in PPMS (Quantum Design) indicated the correct Nb_3Sn stoichiometry and homogeneity in view of their consistently measured $T_c = 17.6\text{ K}$ and $\text{RRR}(300\text{K}/20\text{K}) \sim 4$ between samples across several batches, which was corroborated by the vibrational sample magnetometer in PPMS measurements. Lastly, the stoichiometry was also checked by the SEM EDX (Hitachi SU3500, Oxford Instruments X-MAX-20).

Figure 1 demonstrates certain physical properties of our films [Figs. 1(a) and 1(b)] and bridges [Figs. 1(c)–1(f)].

Transformation of the films into bridges was performed using a combination of 3D printing (Elegoo Mars-3 printer),

photolithography, and ion milling to achieve macroscopic contact pads on $1 \times 1 \text{ cm}^2$ sapphire substrates. Reactive ion milling (Bal-Tec RES-101, CF_4 etchant) was used to develop a metallic film pattern; see Fig. 1(c). After removal of the resin, the structure was covered by negative photoresist (PKP-308PI, Transene Co., Inc.), and the 100- μm -scale bridge was narrowed down to 12 μm with the projective photolithography (using mask projection via LUMAM epifluorescent microscope, $10\times$ objective). After ion milling, the last stage of patterning was undertaken using positive photoresist (TRANSIST PC800, Transene Co., Inc.) and the same projective technique with the $40\times$ objective and a different mask in the form of two holes. The final ion milling delivered bridges about 10–20 μm long and down to 2 μm wide; see Fig. 1(d).

Ion milling affects the physical properties of bridges, thus reducing the critical temperatures down to the 2–12 K range. This T_c reduction was also noticed in the literature [28]. We were able to restore the T_c values up to 17 K in some of the bridges by high-vacuum postannealing ($\sim 10^{-6}$ Torr) at 900 $^\circ\text{C}$ for 30 min, as shown in Fig. 1(e).

III. RESULTS

The tests demonstrated $|V(I_+)| \neq |V(I_-)|$ [Fig. 1(f)], thus indicating the possibility of an SDE. At various temperatures, this type of the $V(I)$ test was systematically performed on a 2 μm bridge and the results are shown in Fig. 2(a). These measurements confirm the fact mentioned in the literature that at lower temperatures, the difference ΔI between the threshold values of I_+^{res} and I_-^{res} increases with the decreasing bias temperature [5,27] (the value of I_-^{res} corresponds to the current at which the resistive state emerges).

To confirm the expected diode effect, the bridge then was biased at 2 K (PPMS DynaCool cryostat) with external current source and nanovoltmeter (Keithley 6221 and 2182A, respectively) applied at frequency 0.1 Hz. Figure 2(b) demonstrates the result optimized at magnetic field 75 Oe for the 2 μm bridge.

Since superconducting diodes are considered to be important elements for electronics, for the majority of applications, it is meaningful to register the effect at possibly higher frequencies. The Keithley current source that we used generates AC currents up to 100 kHz. The corresponding detection of voltage output was performed by an oscilloscope (Tektronix TDS 644A) using the 5- μm -wide bridge. The results are shown in Figs. 2(c) and 2(d) for 10 and 100 kHz frequencies, respectively. Higher-frequency measurements require specially designed circuitry in the cryostat since noise becomes an issue, as is seen from the comparison of Fig. 2(b) with Figs. 2(c) and 2(d). As visible in Fig. 2(d), sporadic negative and missing spikes emerge at higher frequencies. These are most likely caused by nonadiabatic evolution of the quantum system. Both of these factors lower the amplitude of spikes at the oscilloscope's averaging; in Fig. 2(e), the amplitude is lower at $\sim 175 \text{ mV}$, compared to Figs. 2(c) and 2(d) with the amplitudes $\sim 250 \text{ mV}$. The individual amplitude of the spikes, within the noise limit, is frequency independent and equal to the resistance of the dissipative flux flow motion times the current amplitude.

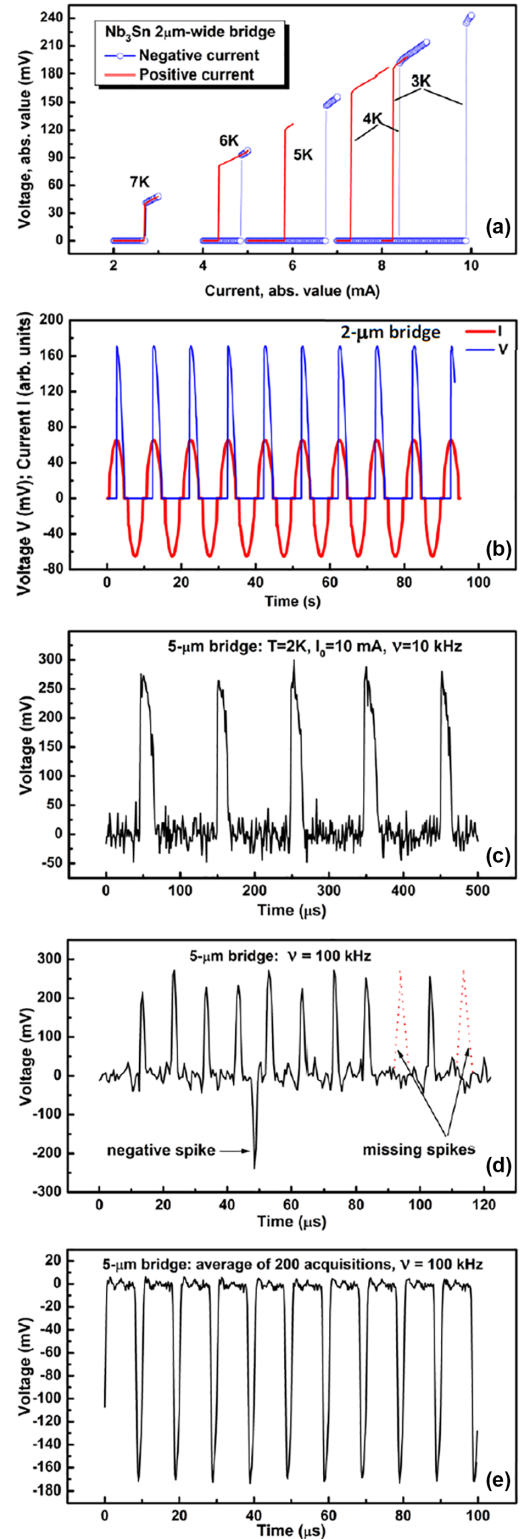


FIG. 2. (a) Resistive state at various values of bias temperature for the applied current of opposite polarities (absolute values are plotted). (b) The SDE in 2 μm bridge at sinusoidal current amplitude $\approx 10 \text{ mA}$ and frequency 0.1 Hz. (c) Same as in (b), with 5- μm -wide bridge at frequency 10 kHz. (d) Same as in (c), at frequency 100 kHz. (e) Average of 200 acquisitions with reversed polarity of the magnetic field. In all cases, a magnetic field orthogonal to the surface of the bridge was applied and optimized in the range 50–100 Oe. Arrows indicate a negative voltage spike and absent spikes (shown also by dotted line) at higher bias frequency.

IV. DISCUSSION

To estimate the frequency range of this type of diode, one needs to understand what the underlying mechanism of the SDE is. As was expected from the general reasons mentioned in Sec. I, the effect is nonexistent in the absence of external magnetic field \mathbf{H}_{ext} . Comparison of Figs. 2(d) and 2(e) shows the change of diode polarity due to the reversal of the external magnetic field from 100 to -100 Oe. The field \mathbf{H}_{ext} is orthogonal to the bridge surface. So is the vector of the internal magnetic field \mathbf{H}_{int} , though only at the lateral (top and bottom) edges of the bridge. This field is generated by the current flow through the bridge, with the field lines circulating it. Thus, from symmetry considerations, for an infinitesimally thin bridge, it is orthogonal to the bridge surface at the top and bottom edges. At one edge, \mathbf{H}_{int} is parallel and, at the other edge, it is antiparallel to \mathbf{H}_{ext} . Thus, on one of these lateral edges, the amplitudes of external and internal fields add up, while on the other edge, they subtract. In the AC case, this adding and subtracting reciprocate periodically with frequency ω ,

$$B = \begin{cases} H_{ext} + H_{int} \sin(\omega t) & \text{for the top edge} \\ H_{ext} - H_{int} \sin(\omega t) & \text{for the bottom edge.} \end{cases} \quad (1)$$

The \mathbf{H}_{ext} field amplitude of ~ 100 Oe is optimal for the SDE in our bridges. Higher values (~ 150 Oe) quench the effect. The resistive state which yields a nonzero voltage in Fig. 2(c) is caused by vortex motion: the corresponding value of the resistance is a fraction of its normal value. This strongly distinguishes our SDE from those via conformal-mapped nanoholes SDE [40], where the normal state transition stands for the resistance, and flux pinning on defects (nanoholes) secures the lossless current flow, and also breaks the IS. In our case, as follows from Fig. 2(c), the resistance (V/I) reaches values of 25–40 Ω . At the same time, full transition to the normal state corresponds to the resistance of ~ 60 Ω . Figure 3 depicts a set of $V(I)$ measurements at various temperatures. Multiple resistivity jumps are noticeable at lower temperature curves. This multiple-jumps feature was noticed with all our bridges, including the 5- μm -width one. The stepwise behavior of the $V(I)$ curves is explained via vortex pattern rearrangement [43–45]. Interestingly, Berdiyorov *et al.* [43] predicted a nonmonotonic behavior of critical current of the transition from a resistive flux-flow state into a normal state (calling this current j_{c3}) for an increase in magnetic field. In our case, a nonmonotonic behavior of j_{c3} is observable with the bias temperature. This fact requires an explanation via modeling; however, it is beyond the scope of this report.

To explain the results shown in Fig. 2, modeling is necessary which, unlike [40], does not involve a transition into the normal state for resistivity. Using COMSOL MULTIPHYSICS, we designed a p -parameter model [46] in which the IS is geometrically broken: the top edge of the strip has a weaker barrier to vortex penetration than the bottom edge. One can assume, as in the case of NbN SDE [28], that the IS is broken by opposite edges asymmetry caused by physical reasons during the bridge preparation. A closer look at the inset of Fig. 1(d) illustrates the fractal structure of the edge of the current-flow channel. Realistically, the opposite edges are not microscop-

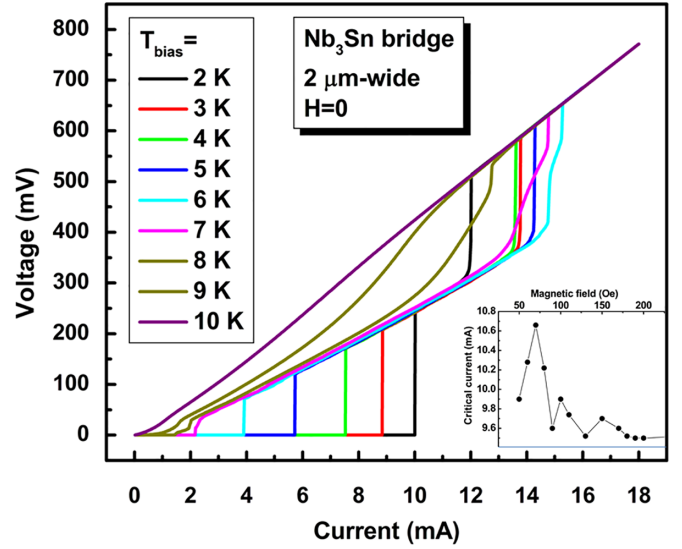


FIG. 3. $V(I)$ dependence of 2- μm -wide bridge. Resistive state jumps are noticeable before the transition to the normal state as well as at the intermediate current. The same resistive jumps, with the intermediate voltage values roughly about half of that in the normal state, have been detected for the 5- μm -width bridge. Inset shows the magnetic field dependence of the critical current for the 2 μm bridge (cf. [27]).

ically symmetric, so our assumption looks quite plausible. Interestingly, in Ref. [27] it is argued that the magnetic field dependence of the nonreciprocal critical current is linear (near the maximum value) when the diode effect is caused by the edge asymmetry. It looks like our experimental observation (see inset to Fig. 3), as well as the modeling data below, are in support of the claim of Ref. [27].

Prior to discussing the details of modeling, we should make one more important remark. Sapphire, which we used as a substrate material, has a very high heat conductivity at low temperatures—much higher than Si, which was used in [40]. This allowed us when modeling to decouple the dynamics of the superconducting electrons from the thermal deviation of the lattice from equilibrium. The lattice just serves as an equilibrium heat sink at some effective temperature T . The system of time-dependent Ginzburg-Landau (TDGL) equations for the Cooper-pair wave function $\Psi = \text{Re}\Psi + i\text{Im}\Psi$ in the dimensionless form can be presented as (see, e.g., [46])

$$\begin{aligned} \dot{\psi}_1 = & \frac{1}{\kappa^2}(\psi_{1,xx} + \psi_{1,yy}) + \frac{2}{\kappa}(A_1\psi_{2,x} + A_2\psi_{2,y}) \\ & + \frac{\psi_2}{\kappa}(A_{1,x} + A_{2,y}) - \psi_1(A_1^2 + A_2^2) \\ & + \psi_1(1 - \psi_1^2 - \psi_2^2 + p), \end{aligned} \quad (2)$$

$$\begin{aligned} \dot{\psi}_2 = & \frac{1}{\kappa^2}(\psi_{2,xx} + \psi_{2,yy}) - \frac{2}{\kappa}(A_1\psi_{1,x} + A_2\psi_{1,y}) \\ & - \frac{\psi_1}{\kappa}(A_{1,x} + A_{2,y}) - \psi_2(A_1^2 + A_2^2) \\ & + \psi_2(1 - \psi_1^2 - \psi_2^2 + p), \end{aligned} \quad (3)$$

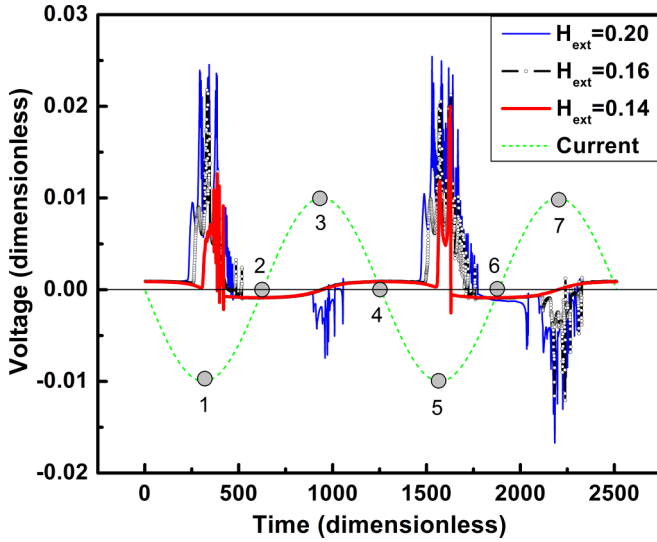


FIG. 4. Voltage across the diode (superconducting bridge) generated by a sinusoidal AC bias: $j = j_0 \sin(\omega t + \pi)$, where π is added for computational convenience. The amplitude of j_0 is chosen to yield $H_{int} = -0.48$. Different curves correspond to different values of external magnetic field H_{ext} .

$$\sigma \dot{A}_1 = -\frac{1}{\kappa}(\psi_2 \psi_{1,x} - \psi_1 \psi_{2,x}) - (\psi_1^2 + \psi_2^2)A_1 + A_{1,yy} - A_{2,xy}, \quad (4)$$

$$\sigma \dot{A}_2 = -\frac{1}{\kappa}(\psi_2 \psi_{1,y} - \psi_1 \psi_{2,y}) - (\psi_1^2 + \psi_2^2)A_2 + A_{2,xx} - A_{1,xy}. \quad (5)$$

Here, $\kappa = \lambda_L(T)/\xi(T)$ is the Ginzburg-Landau parameter, $\sigma = 0.172$ is the dimensionless conductivity, and $\mathbf{A} = \hat{\mathbf{x}}A_1 + \hat{\mathbf{y}}A_2$ is the vector potential (we chose the unit vector $\hat{\mathbf{x}}$ to be along the transport current flow in the strip, with $\hat{\mathbf{y}}$ orthogonal to it). In our notations, a dot over the symbol means time derivative, and a dot before the subindices means derivative over the subindex variables after it. The parameter $p = p(x, y)$, if negative, generates local “weakening” of the superconducting order parameter [46] and, consequently, breaking of the IS. In our model, we chose $p = p(y) = -0.3$ along the top edge within a $\lambda_L(T)$ distance from that edge. Since both superconducting and normal currents are absent across the lateral edges of the strip, we imposed zero-flux conditions for $\partial\Psi/\partial\mathbf{n}$ on these boundaries and periodic boundary conditions on transverse facets (i.e., on the boundaries orthogonal to the current flow). Initial conditions for the Ψ function should not be identically zero; for example, $\psi_1(t=0) = 1$ and $\psi_2(t=0) = 0$ may be chosen. Boundary conditions for the $\hat{\mathbf{y}}$ component of the vector potential \mathbf{A} are also periodic on the transverse facets of the strip. On the lateral edges, they are $\text{curl } \mathbf{A} = \mathbf{B}$, which is implemented via the flux-source conditions. An electric field in the chosen gauge for Eqs. (2)–(5) with the zero scalar potential, $\varphi \equiv 0$, is $\mathbf{E} = -\partial\mathbf{A}/\partial t$, which means that the solution $\mathbf{A} = \mathbf{A}(t)$ is an explicit function of time. As soon as this function is known in the whole 2D volume of the strip, one can average $A_{1,t}$ over this volume and determine, up

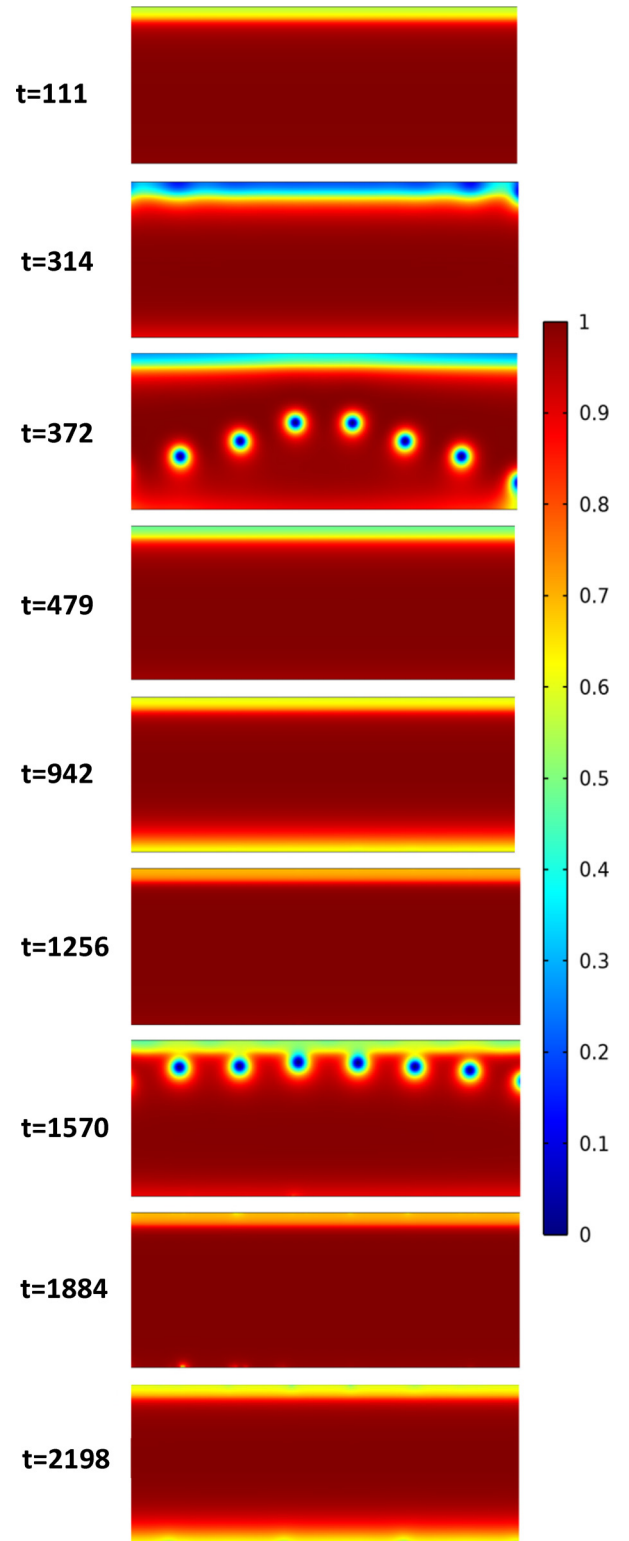


FIG. 5. Physical processes in the active part of the superconducting bridge, resulting in the SDE for $H_{ext} = 0.14$, $H_{int} = -0.48$.

to a constant, the voltage V caused by the transport current between the transverse facets of the strip.

The dimensionless spatial distance in the adopted system of equations corresponds to the London penetration depth, $\lambda_L(T)$, while the dimensionless unit of time $t_0 =$

$\pi \hbar / [8k_B(T_c - T)]$ has picosecond order of magnitude if $T_c \sim 17$ K and $T \sim 2$ K.

The results of the modeling are shown in Fig. 4. Figure 5 explains the physical mechanism behind the behavior of the voltage in Fig. 4. A video file in the Supplemental Material [47] provides more details related to both of these figures.

As follows from Fig. 5, for the initial segment of the periodic current (say, at $t = 111$), no fluxons are in the bridge. The current flow is lossless ($V \approx 0$) and the Cooper-pair density is homogeneous within the bridge except the top edge, where it is weakly suppressed due to the asymmetry caused by the p parameter, mimicking the IS break. In accordance with Eq. (1), the magnetic field in the top edge of the bridge at this time segment is higher than at the bottom. Tuning the amplitude of the current and/or the value of the external field amplitude H_{ext} , one can exceed the critical value of \mathbf{B} at the top edge. This allows vortices to start penetrating from the top edge into the bulk of the bridge. The relative values of H_{ext} and H_{int} should be chosen such that the Lorentz force is strong enough to move these vortices across the bridge during the first half period of $\sin(\omega t)$ function. In the second half period, the value of \mathbf{B} is larger at the bottom edge. However, because the “rigidity” of this edge (i.e., its Bean-Livingston barrier) is higher, the value of \mathbf{B} , which was critical for the top edge, is not enough to also be critical for the bottom edge. So even at $t = 940$, when \mathbf{B} is maximal at the bottom, no vortices penetrate from the bottom (just the density of Cooper pairs changes a bit). This evolution displayed in Fig. 5 occurs at $H_{ext} = 0.14$ (and $H_{int} = -0.48$). If these values are correctly chosen, during the next period the process repeats. In the case of improper choices (e.g., $H_{ext} = 0.16$ or $H_{ext} = 0.20$ with the same $H_{int} = -0.48$), the diode malfunctioning can occur. This kind of behavior was also noticed during the experiments [see Fig. 2(d)].

Associating the SDE with the described vortex motion, we can make certain estimates for the performance limits of the SDE in the frequency domain. In the modeled example, the width of the bridge should constitute units of λ_L . The angular frequency was chosen to be $\omega = 0.005$. It corresponds to frequency $\nu \sim 300$ MHz. This value is in accordance with our experimental observations. The 100 kHz results have been obtained for a 5- μm -wide bridge. If the geometry is scaled down from 5- μm -wide to 5–50-nm-wide bridges, it can deliver frequencies 2–3 orders of magnitude higher (10–100 MHz range)

because of geometric factors affecting their escape time. One can ask: can an even higher frequency range be reached? The answer appears to be yes due to the following reason: the speed of kinematic vortices is three orders of magnitude higher than that of the Abrikosov vortices [48,49]. If the $I_{+/-}^{res}$ asymmetry enters the range of kinematic vortices (the highest current $V(I)$ jump area in Fig. 3 which corresponds to the transition into the normal state), then the operational frequencies of the superconducting diodes can reach 100 GHz. Obviously, more research is required to reach that stage experimentally and more modeling is required for better guidance on how to reach this regime.

V. SUMMARY

We successfully demonstrated the SDE in ordinary thin superconducting μm -size bridges of Nb_3Sn with $T_c = 17$ K. The TRS was broken by external magnetic fields less than 100 Oe, and the IS was broken by structural asymmetry between the bridge edges. High-frequency (up to 100 kHz) diode performance was documented in the time domain and evidence regarding the nonequilibrium flux quanta dynamic mechanism of diode action was obtained. Using this evidence, a qualitative explanation of the diode action was obtained via finite-element modeling using TDGL equations. Based on both our experimental and modeling results, it is possible to conclude that this kind of SDE can be functional at 2–3 orders higher frequencies than the upper limit of our measuring instrument (100 kHz). With the involvement of kinematic vortices into the SDE action, an even higher range of frequencies (of the order of 100 GHz) can be achieved. More experiments guided by modeling can yield two-terminal and multiterminal [50] high-performance devices for superconducting electronics.

ACKNOWLEDGMENTS

The work of the Chapman University research team is supported by the ONR Grants No. N00014-21-1-2879 and No. N00014-20-1-2442. We are grateful to the Physics Art Frontiers for the provided technical assistance. We would like to express our gratitude to R. Dulal for his assistance at the initial stage of this research and to the anonymous referees of this article for their valuable comments.

- [1] A. M. Gulian, V. R. Nikoghosyan, E. D. Gulian, and G. G. Melkonyan, Quasilocally action of curl-less vector potential on vortex dynamics in superconductors, *Phys. Lett. A* **382**, 1058 (2018).
- [2] Y. Tokura and N. Nagaosa, Nonreciprocal responses from non-centrosymmetric quantum materials, *Nat. Commun.* **9**, 3740 (2018).
- [3] R. Wakatsuki and N. Nagaosa, Nonreciprocal Current in Non-centrosymmetric Rashba Superconductors, *Phys. Rev. Lett.* **121**, 026601 (2018).
- [4] S. Hoshino, R. Wakatsuki, K. Hamamoto, and N. Nagaosa, Nonreciprocal charge transport in two-dimensional noncentrosymmetric superconductors, *Phys. Rev. B* **98**, 054510 (2018).

- [5] F. Ando, Y. Miyasaka, T. Li, J. Ishizuka, T. Arakawa, Y. Shiota, T. Moriyama, Y. Yanase, and T. Ono, Observation of superconducting diode effect, *Nature (London)* **584**, 373 (2020).
- [6] T. Ideue and Y. Iwasa, One-way supercurrent achieved in an electrically polar film, *Nature (London)* **584**, 349 (2020).
- [7] C. Baumgartner, L. Fuchs, A. Costa, S. Reinhardt, S. Gronin, G. C. Gardner, T. Lindemann, M. J. Manfra, P. E. Faria Junior, D. Kochan, J. Fabian, N. Paradiso, and C. Strunk, Supercurrent rectification and magnetochiral effects in symmetric Josephson junctions, *Nat. Nanotechnol.* **17**, 39 (2022).
- [8] H. Wu, Y. Wang, Y. Xu, P. K. Sivakumar, C. Pasco, U. Filippozzi, S. S. P. Parkin, Y.-J. Zeng, T. McQueen, and M. N.

- Ali, The field-free Josephson diode in a van der Waals heterostructure, *Nature (London)* **604**, 653 (2022).
- [9] E. Strambini, M. Spies, N. Ligato, S. Ilić, M. Rouco, C. González-Orellana, M. Ilyn, C. Rogero, F. S. Bergeret, J. S. Moodera, P. Virtanen, T. T. Heikkilä, and F. Giazotto, Superconducting spintronic tunnel diode, *Nat. Commun.* **13**, 2431 (2022).
- [10] T. Morimoto and N. Nagaosa, Nonreciprocal current from electron interactions in noncentrosymmetric crystals: Roles of time reversal symmetry and dissipation, *Sci. Rep.* **8**, 2973 (2018).
- [11] H. Isobe, S.-Y. Xu, and L. Fu, High-frequency rectification via chiral Bloch electrons, *Sci. Adv.* **6**, eaay2497 (2020).
- [12] Y. M. Itahashi, T. Ideue, S. Hoshino, C. Goto, H. Namiki, T. Sasagawa, and Y. Iwasa, Giant second harmonic transport under time-reversal symmetry in a trigonal superconductor, *Nat. Commun.* **13**, 1659 (2022).
- [13] We are grateful to the anonymous referee who invited our attention to this issue.
- [14] R. Wakatsuki, Y. Saito, S. Hoshino, Y. M. Itahashi, T. Ideue, M. Ezawa, Y. Iwasa, and N. Nagaosa, Nonreciprocal charge transport in noncentrosymmetric superconductors, *Sci. Adv.* **3**, e1602390 (2017).
- [15] J. Shin, S. Son, J. Yun, G. Park, K. Zhang, Y. J. Shin, J.-G. Park, and D. Kim, Magnetic proximity-induced superconducting diode effect and infinite magnetoresistance in van der Waals heterostructure, *arXiv:2111.05627*.
- [16] C. Baumgartner, L. Fuchs, A. Costa, J. Picó-Cortés, S. Reinhardt, S. Gronin, G. C. Gardner, T. Lindemann, M. J. Manfra, P. E. F. Junior, D. Kochan, J. Fabian, N. Paradiso, and C. Strunk, Effect of Rashba and Dresselhaus spin-orbit coupling on supercurrent rectification and magnetochiral anisotropy of ballistic Josephson junctions, *J. Phys.: Condens. Matter* **34**, 154005 (2022).
- [17] L. Bauriedl, C. Bäuml, L. Fuchs, C. Baumgartner, N. Paulik, J. M. Bauer, K.-Q. Lin, J. M. Lupton, T. Taniguchi, K. Watanabe, C. Strunk, and N. Paradiso, Supercurrent diode effect and magnetochiral anisotropy in few-layer NbSe₂, *Nat. Commun.* **13**, 4266 (2022).
- [18] N. F. Q. Yuan and L. Fu, Supercurrent diode effect and finite-momentum superconductors, *Proc. Natl. Acad. Sci.* **119**, e2119548119 (2022).
- [19] J. J. He, Y. Tanaka, and N. Nagaosa, A phenomenological theory of superconductor diodes, *New J. Phys.* **24**, 053014 (2022).
- [20] J.-X. Lin, P. Siriviboon, H. D. Scammell, S. Liu, D. Rhodes, K. Watanabe, T. Taniguchi, J. Hone, M. S. Scheurer, and J. I. A. Li, Zero-field superconducting diode effect in small-twist-angle trilayer graphene, *Nat. Phys.* **18**, 1221 (2022).
- [21] S. Ilić and F. S. Bergeret, Theory of the Supercurrent Diode Effect in Rashba Superconductors with Arbitrary Disorder, *Phys. Rev. Lett.* **128**, 177001 (2022).
- [22] T. Karabassov, I. V. Bobkova, A. A. Golubov, and A. S. Vasenko, Hybrid helical state and superconducting diode effect in superconductor/ferromagnet/topological insulator heterostructures, *Phys. Rev. B* **106**, 224509 (2022).
- [23] A. Daido, Y. Ikeda, and Y. Yanase, Intrinsic Superconducting Diode Effect, *Phys. Rev. Lett.* **128**, 037001 (2022).
- [24] M. S. Anwar, T. Nakamura, R. Ishiguro, S. Arif, J. W. A. Robinson, S. Yonezawa, M. Sigrist, and Y. Maeno, Spontaneous superconducting diode effect in nonmagnetic Nb/Ru/Sr₂RuO₄ topological junctions, *arXiv:2211.14626*.
- [25] R. S. Souto, M. Leijnse, and C. Schrade, The Josephson Diode Effect In Supercurrent Interferometers, *Phys. Rev. Lett.* **129**, 267702 (2022).
- [26] K. Halterman, M. Alidoust, R. Smith, and S. Starr, Supercurrent diode effect, spin torques, and robust zero-energy peak in planar half-metallic trilayers, *Phys. Rev. B* **105**, 104508 (2022).
- [27] Y. Hou, F. Nichele, H. Chi, A. Lodesani, Y. Wu, M. F. Ritter, D. Z. Haxell, M. Davydova, S. Ilić, O. Glezakou-Elbert, A. Varambally, F. S. Bergeret, A. Kamra, L. Fu, P. A. Lee, and J. S. Moodera, Ubiquitous superconducting diode effect in superconductor thin films, *arXiv:2205.09276*.
- [28] D. Suri, A. Kamra, T. N. G. Meier, M. Kronseder, W. Belzig, C. H. Back, and C. Strunk, Non-reciprocity of vortex-limited critical current in conventional superconducting microbridges, *Appl. Phys. Lett.* **121**, 102601 (2022).
- [29] M. K. Hope, M. Amundsen, D. Suri, J. S. Moodera, and A. Kamra, Interfacial control of vortex-limited critical current in type-II superconductor films, *Phys. Rev. B* **104**, 184512 (2021).
- [30] D. Y. Vodolazov and F. M. Peeters, Superconducting rectifier based on the asymmetric surface barrier effect, *Phys. Rev. B* **72**, 172508 (2005).
- [31] V. V. Shmidt, The critical current in superconducting films, *Sov. Phys. JETP* **30**, 1137 (1970).
- [32] V. V. Shmidt, Critical currents in superconductors, *Sov. Phys. Usp.* **13**, 408 (1970).
- [33] C. P. Bean and J. D. Livingston, Surface Barrier in Type-II Superconductors, *Phys. Rev. Lett.* **12**, 14 (1964).
- [34] K. Fossheim and A. Sudbø, *Superconductivity: Physics and Applications* (John Wiley and Sons Ltd, England, 2004), pp. 232–233.
- [35] J. E. Villegas, S. Savel'ev, F. Nori, E. M. Gonzalez, J. V. Anguita, R. García, and J. L. Vicent, A Superconducting Reversible Rectifier That Controls the Motion of Magnetic Flux Quanta, *Science* **302**, 1188 (2003).
- [36] J. E. Villegas, E. M. Gonzalez, M. P. Gonzalez, J. V. Anguita, and J. L. Vicent, Experimental ratchet effect in superconducting films with periodic arrays of asymmetric potentials, *Phys. Rev. B* **71**, 024519 (2005).
- [37] C. C. de Souza Silva, J. Van de Vondel, M. Morelle, and V. V. Moshchalkov, Controlled multiple reversals of a ratchet effect, *Nature (London)* **440**, 651 (2006).
- [38] Q. Lu, C. J. Olson Reichhardt, and C. Reichhardt, Reversible vortex ratchet effects and ordering in superconductors with simple asymmetric potential arrays, *Phys. Rev. B* **75**, 054502 (2007).
- [39] T. Ideue, S. Koshikawa, H. Namiki, T. Sasagawa, and Y. Iwasa, Giant nonreciprocal magnetotransport in bulk trigonal superconductor PbTaSe₂, *Phys. Rev. Res.* **2**, 042046 (2020).
- [40] Y.-Y. Lyu, J. Jiang, Y.-L. Wang, Z.-L. Xiao, S. Dong, Q.-H. Chen, M. V. Milošević, H. Wang, R. Divan, J. E. Pearson, P. Wu, F. M. Peeters, and W.-K. Kwok, Superconducting diode effect via conformal-mapped nanoholes, *Nat. Commun.* **12**, 2703 (2021).
- [41] C. S. Sundahl, Synthesis of Superconducting Nb₃Sn Thin Film Heterostructures for the Study of High-Energy RF Physics, Ph.D. thesis (The University of Wisconsin - Madison, Madison, WI, 2019), ProQuest Dissertations Publishing, No. 13805402.
- [42] J. P. Charlesworth, I. Macphail, and P. E. Madsen, Experimental work on the niobium-tin constitution diagram and related studies, *J. Mater. Sci.* **5**, 580 (1970).

- [43] G. R. Berdiyrov, A. K. Elmurodov, F. M. Peeters, and D. Y. Vodolazov, Finite-size effect on the resistive state in a mesoscopic type-II superconducting stripe, *Phys. Rev. B* **79**, 174506 (2009).
- [44] P. Sánchez-Lotero, J. Albino Aguiar, and D. Domínguez, Behavior of the flux-flow resistivity in mesoscopic superconductors, *Physica C* **503**, 120 (2014).
- [45] D. Y. Vodolazov and F. M. Peeters, Rearrangement of the vortex lattice due to instabilities of vortex flow, *Phys. Rev. B* **76**, 014521 (2007).
- [46] A. Gulian, *Shortcut to Superconductivity: Superconducting Electronics via COMSOL Modeling* (Springer Nature, Switzerland, 2020).
- [47] See Supplemental Material at <http://link.aps.org/supplemental/10.1103/PhysRevB.107.054506> for the dynamic illustration of Fig. 4 and Fig. 5.
- [48] A. Weber and L. Kramer, Dissipative states in a current-carrying superconducting film, *J. Low Temp. Phys.* **84**, 289 (1991).
- [49] A. Andronov, I. Gordion, V. Kurin, I. Nefedov, and I. Shereshevsky, Kinematic vortices and phase slip lines in the dynamics of the resistive state of narrow superconductive thin film channels, *Physica C* **213**, 193 (1993).
- [50] S. Chahid, S. Teknowijoyo, and A. Gulian, Quadristor: A novel device for superconducting electronics, [arXiv:2211.13340](https://arxiv.org/abs/2211.13340).